

Binary classification of spoken words with passive elastic metastructures

Tena Dubček,¹ Daniel Moreno-Garcia,² Thomas Haag,³ Henrik R. Thomsen,³ Theodor S. Becker,³ Christoph Bärlocher,³ Fredrik Andersson,³ Sebastian D. Huber,¹ Dirk-Jan van Manen,³ Luis Guillermo Villanueva,² Johan O.A. Robertsson,³ and Marc Serra-Garcia^{3,4}

¹*Institute for Theoretical Physics, ETH Zürich, 8093 Zürich, Switzerland*

²*School of Engineering, EPFL, 1015 Lausanne, Switzerland*

³*Institute for Geophysics, ETH Zürich, 8092 Zürich, Switzerland*

⁴*AMOLF, Science Park 104, 1098 XG Amsterdam, the Netherlands*

(Dated: November 17, 2021)

Many electronic devices spend most of their time waiting for a wake-up event: pacemakers waiting for an anomalous heartbeat, security systems on alert to detect an intruder, smartphones listening for the user to say a wake-up phrase. These devices continuously convert physical signals into electrical currents that are then analyzed on a digital computer—leading to power consumption even when no event is taking place. Solving this problem requires the ability to passively distinguish relevant from irrelevant events (e.g. tell a wake-up phrase from a regular conversation). Here, we experimentally demonstrate an elastic metastructure, consisting of a network of coupled silicon resonators, that passively discriminates between pairs of spoken words—solving the wake-up problem for scenarios where only two classes of events are possible. This passive speech recognition is demonstrated on a dataset from speakers with significant gender and accent diversity. The geometry of the metastructure is determined during the design process, in which the network of resonators (*mechanical neurones*) learns to selectively respond to spoken words. Training is facilitated by a machine learning model that reduces the number of computationally expensive three-dimensional elastic wave simulations. By embedding event detection in the structural dynamics, mechanical neural networks thus enable novel classes of always-on smart devices with no standby power consumption.

A tuning fork resonates when a tone of the corresponding pitch is played nearby [Fig. 1a], a swing reaches higher points when pushed periodically at a frequency determined by its length, and atoms are excited by light with a frequency given by the energy of an electronic transition [1, 2]. Resonance—the phenomenon where a physical system responds strongly to signals of a particular (resonant) frequency—is often used in technological applications, such as the frequency filters in cell phones. While it is well understood that resonances allow us to passively distinguish between signals using frequency as a criterion, here we ask if it is possible to fabricate structures that distinguish between signals according to more complex criteria [Fig. 1b]—for example, that react only to particular spoken words. Can we combine mechanical elements, such as masses and springs, to achieve precise signal processing comparable to that done in electronic circuits, introducing a field that we refer to as *springtronics*? Can we build elastic devices that passively implement intelligent behaviour?

Recent theoretical proposals suggest that the answer to these questions is indeed affirmative, and mass-spring-damper systems are in fact capable of complex computation [3, 4]. In this letter, we experimentally demonstrate passive *springtronic* speech processing by realising an elastic metastructure [Fig. 1c] that discriminates between pairs of spoken words. The center of the structure vibrates with high amplitude when excited with one of the words but not the other, thus performing a machine learning classification task [5]. Our experiments only involve structures vibrating in the linear response

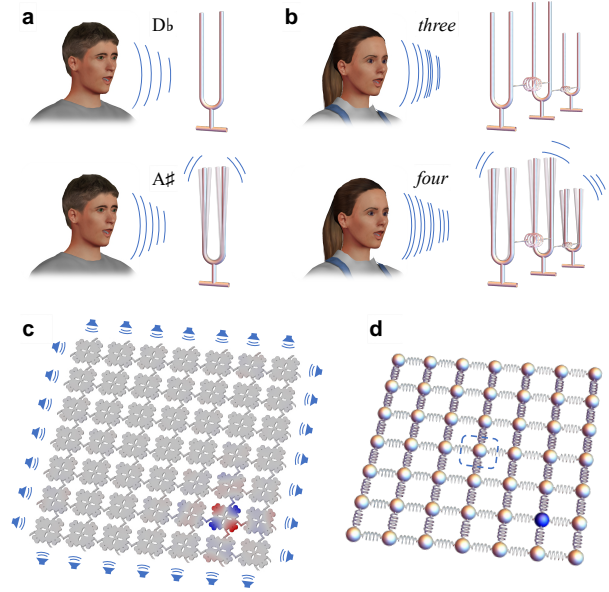


FIG. 1. Passive speech recognition | **a** A resonator discriminates between frequencies. **b** Our metastructure of coupled resonators discriminates between spoken digits. **c** The metastructure is a lattice of vibrating plates connected by beams, with a geometry (beam locations and hole sizes) optimized to achieve the desired selective response. **d** The structure is modelled as a mass-spring model. Each mass corresponds to a vibration localised around a plate. The blue mass corresponds to the displacement represented by the coloring in panel c.

regime. Remarkably, our findings show that even in the linear regime, passive elastic structures are able to solve binary classification tasks with accuracies exceeding 90 %. This number does not represent a ceiling to the speech processing performance of elastic structures. Including nonlinearity can result in improved accuracies, as discussed at the end of the paper. Our observations on a metastructure that performs complex classification tasks can be intuitively understood by drawing a parallel between the resonator network that constitutes the metastructure [Fig. 1d] and the biologically-inspired artificial neural networks (ANNs) commonly used in machine learning [6, 7]. The high quality factor characteristic of mechanical resonators (Here, $Q \approx 10^3$, but some realisations reach $Q \approx 10^9$ [8]), provides *springtronic* implementations of neuromorphic computing with a very long memory and therefore with the capability to recognise complex patterns in time.

Prior works designing mechanical structures with tailored dynamical responses are based on transforma-

tion optics [9], homogenisation [10], topological waveguiding [11], and combinatorics [12, 13] among others. Generally, due to the complexity of the design problem, these studies have focused on periodic or smoothly-varying designs, with completely aperiodic systems considered only in the quasi-static case [12, 13]. This is related to the computational cost of simulating the designs: A periodic system can be optimised by simulating a single unit cell (on the order of 10^5 degrees of freedom, DOFs) under Bloch boundary conditions, while a non-periodic design requires simulating the complete lattice. Neural networks for speech recognition are inherently aperiodic and transient, therefore, a full FEM simulation for a network with 10^2 neurones requires solving for 10^5 DOFs for every time step (here, $n_{steps} \approx 10^5$) of every training sample (here, $n_{samples} \approx 10^3$), and determining the gradient of the transmitted energy with respect to the network geometry. As a consequence of this computational cost, directly optimising the structural geometry is impractical.

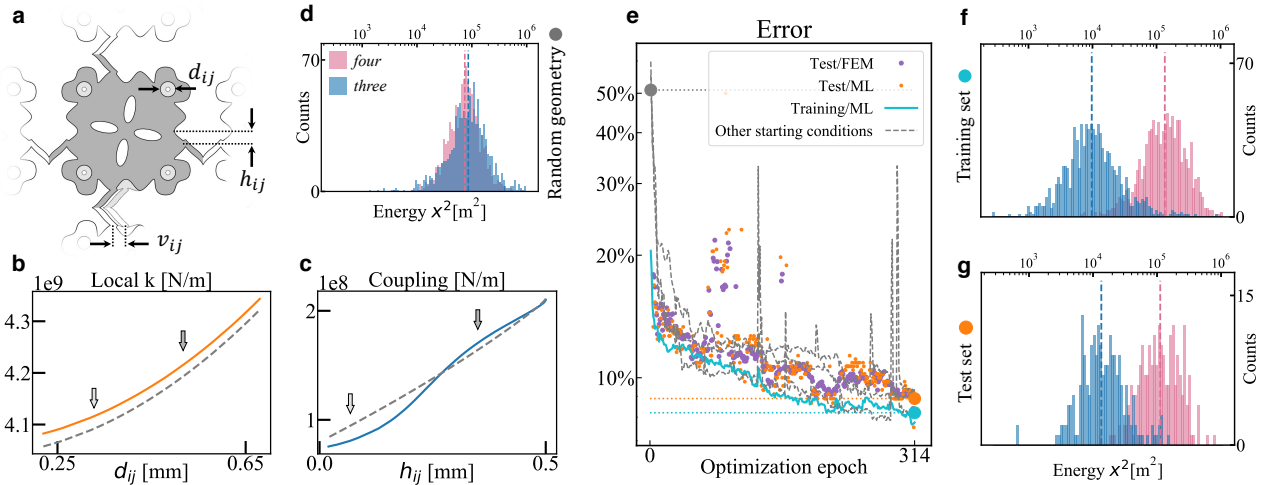


FIG. 2. Sample design | **a** We optimise the geometry by adjusting hole sizes and beam locations. Each unit cell (i, j) contains four holes of equal diameter d_{ij} . The location of the coupling beams is parameterised by h_{ij} and v_{ij} **b** Local stiffness and **c** coupling strength as a function of the hole diameters d_{ij} and beam locations h_{ij} , respectively. The approximation obtained by the ML model is shown with gray dashed lines. A small beam displacement causes a large shift in the coupling constant, because the coupling is strongly suppressed when the beam is placed at the boundary centre, where the plate eigenmode has a node (see Fig. 1c). The dark and pale grey arrows denote the points corresponding to the dark and pale shapes in **a**. **d** Simulated binary classification performance of a structure with randomly chosen geometrical parameters $\{d_{ij}, h_{ij}, v_{ij}\}$. **e** Binary classification error rate evolution during training. The error rate is calculated on the training (lines) and test (dots) sets. We evaluate the test-set performance using full-lattice FEM simulations and using the approximate machine learning model. The training-set performance is only evaluated using the machine learning model. The optimized geometry is predicted to have an accuracy of **f** 91.8% on the training set and **g** 91.1% on the test set.

In this work, we design the metastructure—a 7×7 lattice of coupled silicon vibrating plate resonators [Fig. 1c]—using gradient descent, with gradients determined by the backpropagation algorithm [14, 15]. The plates [Fig. 2a] have holes of varying size that allow

us to adjust the resonant frequency [Fig. 2a,b], and arms whose position determines the strength of coupling to the neighbors [Fig. 2a,c]. The hole diameters and coupling beam positions for each plate are optimised to achieve selectively large vibration amplitudes at the center of the

lattice, when the boundary is excited by a target spoken word. We overcome the computational challenge of gradient determination by mapping the continuous structure to an effective discrete model of masses and springs [Fig. 1d], and constructing a differentiable machine learning (ML) algorithm to predict the mass-spring values from the lattice geometry. We fabricate the designed metastructure using silicon micromachining; the experimental sample closely approaches the theoretically predicted classification accuracy.

We determine the effective mass-spring model for our structure by following the perturbative metamaterials approach [16]. We construct a description using one DOF per lattice site. These DOFs are related to the normal modes of the resonators by the Schrieffer-Wolff transformation [16–18], and correspond to vibrations localized [19] at every individual plate [Fig. 1c,d]. Encoding the lattice dynamics in a 49 DOF mass-spring model, represented by 49×49 mass M and stiffness K matrices, drastically speeds up computations. With this compact model, we simulate the lattice transient dynamics using each training sample as input to the model. Then, we determine the gradient of the transmitted energy with respect to the mass-spring model parameters using back-propagation in time [14, 15]. Since the equivalence between plates and harmonic oscillators is valid only for a limited range of frequencies, we modulate the excitation signal on a high frequency carrier of 72 kHz. Passively generating the modulation carrier is outside the scope of this work, and we refer the reader to elastic structures that generate narrow-band oscillations from broadband acoustic signals [20].

To perform gradient optimisation, we need to know how the vibrational energy in the central plate depends on the lattice geometry (49 hole diameters d_{ij} , 56 horizontal beam locations h_{ij} and 56 vertical beam locations v_{ij}). Applying backpropagation on the mass-spring model tells us how this energy changes when the effective masses and springs are changed. Therefore, we need to translate the calculated changes in the mass-spring model to changes in the lattice geometry. We accomplish this translation by using a differentiable ML model (see Methods) that predicts the relation between the geometric parameters and the equivalent mass-spring system [Fig. 2b,c]. The ML model computes effective models much faster than through full FEM simulation. It also smooths out the dependence of the mass-spring matrices M , K [Fig. 2c] on the geometric parameters d_{ij} , h_{ij} , and v_{ij} , therefore *convexifying* the loss function landscape. Using ML models to replace computationally expensive simulations is an emerging trend in metamaterial research [21, 22].

We train the sample to distinguish between utterances of numbers *three* and *four*, choosing *four* to be our wake-up word. Training is performed on a dataset consisting of 2048 samples, $N_{\text{three}} = 1024$ and $N_{\text{four}} = 1024$, selected from the GoogleTM Speech Commands Dataset [23]. The dataset contains recordings of a large and diverse group of speakers under real-life conditions. We reproduce the recordings 6.8 times faster than realtime, to match the signal bandwidth to our metamaterial platform [24]. The choice of performing the experiment at a higher-than-realtime speed is made for fabrication convenience and does not indicate a fundamental limit of the technology.

We define the training loss function by applying a sigmoidal function [25] to the energy transmitted to the center of the lattice,

$$L = \sum_{q \in \text{threes}} \left[1 + e^{\gamma(E_q - E_T)} \right]^{-1} - \sum_{q \in \text{fours}} \left[1 + e^{\gamma(E_q - E_T)} \right]^{-1},$$

where E_q is the transmitted energy for each sample q , γ is a parameter determining the steepness of the sigmoidal function, and E_T is the threshold separating a *three* from a *four*. In a practical device, the threshold energy E_T would be given by the vibration amplitude necessary to trigger an amplitude-dependent switch [26].

Starting from a random configuration, presenting poor classification performance [Fig. 2d], we minimise the loss using the Broyden-Fletcher-Goldfarb-Shanno (BFGS) algorithm [27], a quasi-Newton method, on batches containing the full training dataset [28] [Fig. 2e]. The optimisation process, consisting of 300 iterations, is repeated for 15 initial configurations. The optimised design that performs best on the training dataset is selected for fabrication. Full-batch BFGS is known to produce higher training accuracies, but to be significantly more affected by overfitting than mini-batch methods, which stochastically select a different subset of training data at each iteration. We did not observe any decrease in generalisation performance due to our choice of optimisation algorithm—the observed degradation was less than 1% between training and test datasets [Fig. 2f,g].

Using an ML model instead of a full FEM simulation drastically improves the optimisation speed. However, the resulting M and K matrices have limited accuracy [Fig. 2b,c]. To address this problem, we perform a full-lattice FEM simulation every 30 BFGS iterations, and shift the matrices predicted by the ML model by $\Delta K = \alpha(K_{\text{FEM}} - K_{\text{ML}})$ and $\Delta M = \alpha(M_{\text{FEM}} - M_{\text{ML}})$. The parameter α is introduced to prevent oscillation; as the optimisation progresses, α is increased smoothly from 0 to 1. The combination of ML predictions with infrequent but exact FEM simulations results in a highly accurate final design.

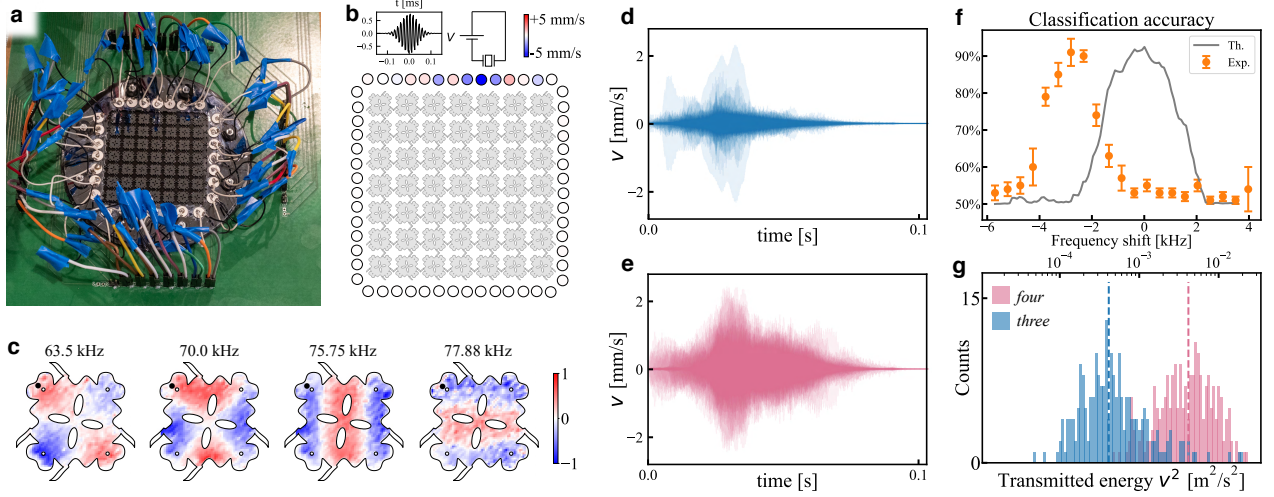


FIG. 3. Experimental realisation | **a** Experimental setup (photography by Astrid Robertsson) **b** Localized edge response measured at 56 points on the sample edge, after driving it by a single piezoelectric actuator. Later, all actuators are driven simultaneously with modulated recordings of spoken words, which provides a uniformly-moving sample boundary condition **c** Measured plate vibrations under harmonic excitation at different frequencies. The black dot represents the point where the neural network output is taken. **d** Superimposed measurements of the plate vibration at the measurement point (band-limited to 62.5 – 74.5 kHz), excited with each of the spoken *three* and **e** *four* sound files in the training dataset. The signals corresponding to *three* present a lower vibration amplitude. **f** Classification accuracy as a function of modulation frequency. **g** Transmitted energy distribution, calculated from the individual curves in **c,d**.

We fabricate the sample [Fig. 3a] on a 380 μm silicon wafer using standard photolithography and etching techniques (See Methods). To impose fixed boundary conditions, the wafer is clamped between two rigid frames.

To approximate the uniform boundary excitation used in the design process, we install 28 thickness-mode piezoelectric actuators. Each piezoelectric actuator produces a localised excitation at the boundary of the sample [Fig. 3b]. We calibrate the actuators by sending Gaussian pulses and determining the transfer function to produce a spatially uniform frequency-independent excitation (See Methods). We measure the vibration of the plates using a scanning Laser Doppler Vibrometer (LDV) [Fig. 3c]. The transmission measurements are done with the LDV pointed at the center site, along the plate diagonal, where the next high-order mode has a node [Fig. 3c], to minimise the influence of unaccounted lattice degrees of freedom. To further ensure that there are no contributions from higher-order modes, we band-limit the measurement to the range of 62.5 – 74.5 kHz (note that such band limiting can be performed trivially in the mechanical domain using a passive band-gap metamaterial). The sample is excited by a harmonic signal, amplitude-modulated by sound recordings from the test dataset. Under these conditions, we measure the transmitted vibration [Fig. 3d,e]. The measurements show a significantly larger center plate vibration when the lattice is excited by a *four*—even though all excitation signals are normalised to have the same energy. To achieve the pre-

dicted classification accuracy, we have to decrease the modulation frequency by 2.8 kHz [Fig. 3f]. This deviation can be accounted by the manufacturing tolerance in the thickness of the wafer, which is nominally $\pm 10 \mu\text{m}$, and can be corrected by trimming the sample after fabrication [29]. With the optimal modulation frequency as determined on the training set [Fig. 3f], we measured a test-set classification accuracy of 89.5% [Fig. 3g], close to the simulated value of 91%.

We finally verify that the proposed approach can be applied to words other than *three* and *four*. For this purpose, we design metastructures to distinguish between all pairs of numbers between 1 and 4 [Fig. 4]. We are able to find designs with high classification accuracies for all but one of the word pairs. This is a striking result, given that the metastructure under consideration is linear and consists of only 49 resonators.

The linear classification performance does not set an ultimate limit on the computational capabilities of passive elastic structures. Even with our limited dataset, including a nonlinear term in the system (See Methods) increased the classification accuracy of the worst-performing word pair by 12% [Fig. 4], while additional nonlinear terms did not further improve the accuracy. The saturation in our nonlinear model is a consequence of overfitting, which becomes relevant due to the much larger number of free parameters in the nonlinear model. The problem of overfitting is known to particularly affect end-to-end trained models [30], and can be mitigated

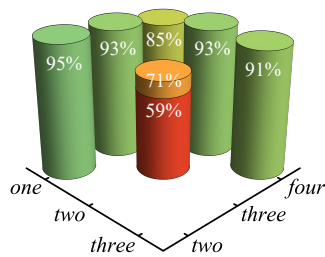


FIG. 4. Generalisation to other word pairs | Theoretical results show that high-performance lattices can be designed for all considered pairs of numbers, except for *two-three*. Performance can be further improved by using nonlinear lattices. The improvement as a consequence of adding a single nonlinear term is shown for the *two-three* pair.

by increasing the dataset size, using regularisation approaches such as dropout [31], or implementing feature extraction [32]. Nevertheless, the theorem by Boyd and Chua [33] guarantees that any fading-memory system can be expressed by a combination of linear dynamical systems and static nonlinear functions. Speech recognition—including large vocabulary speech recognition—is by definition fading-memory, as the output cannot depend on inputs that took place longer ago than the duration of the detected keyword. The flexibility in engineering complex linear responses using elastic metastructures that we have introduced in this work, combined with existing results in the design of nonlinear springs [34], demonstrates a pathway towards the realisation of always-on, smart devices with zero standby power consumption.

ACKNOWLEDGEMENTS

We thank Matija Varga, Miguel Molerón-Bermudez, Sander Tans and Martin van Hecke for enlightening discussions. We are grateful to Sven Friedel at COMSOL multiphysics for help with the meshing of our FEM models. This work was supported by the European Research Council (ERC) under the European Union’s Horizon 2020 Research and Innovation Programme (Grant Agreements No. 694407 and No. 771503).

Correspondence can be addressed to Tena Dubček (dubcekt@ethz.ch) and Marc Serra Garcia (m.serragarcia@amolf.nl).

- [1] J. Bleck-Neuhaus, “Mechanical resonance: 300 years from discovery to the full understanding of its importance,” (2018), arXiv:1811.08353.
- [2] M. Buchanan, “Going into resonance,” (2019).
- [3] M. Serra-Garcia, *Physical Review E* **100** (2019), 10.1103/PhysRevE.100.042202, arXiv:1906.05846.
- [4] J. C. Coulombe, M. C. A. York, and J. Sylvestre, arXiv, 1 (2017).
- [5] N. Matloff, *Statistical Regression and Classification* (2017), 10.1201/9781315119588.
- [6] Y. Lecun, Y. Bengio, and G. Hinton, “Deep learning,” (2015).
- [7] T. Mikolov, A. Deoras, D. Povey, L. Burget, and J. Černocký, in *2011 IEEE Workshop on Automatic Speech Recognition and Understanding, ASRU 2011, Proceedings* (2011) pp. 196–201.
- [8] A. H. Ghadimi, S. A. Fedorov, N. J. Engelsens, M. J. Bereyhi, R. Schilling, D. J. Wilson, and T. J. Kippenberg, *Science* **360**, 764 (2018), <https://www.science.org/doi/pdf/10.1126/science.aar6939>.
- [9] S. A. Cummer, J. Christensen, and A. Alù, *Nature Reviews Materials* **1**, 1 (2016).
- [10] M. Yang, G. Ma, Y. Wu, Z. Yang, and P. Sheng, *Phys. Rev. B* **89**, 064309 (2014).
- [11] S. D. Huber, “Topological mechanics,” (2016).
- [12] C. Coulais, E. Teomy, K. De Reus, Y. Shokef, and M. Van Hecke, *Nature* **535**, 529 (2016), arXiv:1608.00625.
- [13] C. Schumacher, B. Bickel, J. Rys, S. Marschner, C. Daraio, and M. Gross, *ACM Trans. Graph.* **34** (2015), 10.1145/2766926.
- [14] P. J. Werbos, *Neural networks* **1**, 339 (1988).
- [15] M. Hermans, B. Schrauwen, P. Bienstman, and J. Dambre, *PLOS ONE* **9**, 1 (2014).
- [16] K. H. Matlack, M. Serra-Garcia, A. Palermo, S. D. Huber, and C. Daraio, *Nature Materials* **17**, 323 (2018).
- [17] J. R. Schrieffer and P. A. Wolff, *Phys. Rev.* **149**, 491 (1966).
- [18] S. Bravyi, D. P. DiVincenzo, and D. Loss, *Annals of Physics* **326**, 2793 (2011).
- [19] N. Marzari, A. A. Mostofi, J. R. Yates, I. Souza, and D. Vanderbilt, *Reviews of Modern Physics* **84**, 1419 (2012), arXiv:1112.5411.
- [20] M. Serra-Garcia, A. Foehr, M. Molerón, J. Lydon, C. Chong, and C. Daraio, *Phys. Rev. Lett.* **117**, 010602 (2016).
- [21] L. Wang, J. Boddapati, K. Liu, P. Zhu, C. Daraio, and W. Chen, “Mechanical cloak via data-driven aperiodic metamaterial design,” (2021), arXiv:2107.13147 [physics.app-ph].
- [22] L. Wang, Y.-C. Chan, F. Ahmed, Z. Liu, P. Zhu, and W. Chen, *Computer Methods in Applied Mechanics and Engineering* **372**, 113377 (2020).
- [23] P. Warden, “Speech commands: A dataset for limited-vocabulary speech recognition,” (2017).
- [24] M. Serra-Garcia, V. Peri, R. Süssstrunk, O. R. Bilal, T. Larsen, L. G. Villanueva, and S. D. Huber, *Nature* **555**, 342 (2018), arXiv:1708.05015.
- [25] J. S. Bridle, in *Neurocomputing*, edited by F. F. Soulié and J. Héroult (Springer Berlin Heidelberg, Berlin, Heidelberg, 1990) pp. 227–236.
- [26] J. J. Bernstein, M. G. Bancu, E. H. Cook, A. E. Duwel, R. D. Elliott, D. A. Gauthier, S. L. Golmon, J. J. LeBlanc, M. J. Tomaino-Iannucci, J. S. Ung, and M. S. Weinberg, *Journal of Microelectromechanical Systems* **27**, 625 (2018).

[1] J. Bleck-Neuhaus, “Mechanical resonance: 300 years from discovery to the full understanding of its importance,”

- [27] R. Fletcher, *Practical methods of optimization* (John Wiley & Sons, 2013).
- [28] R. Battiti and F. Masulli, “Bfgs optimization for faster and automated supervised learning,” in *International Neural Network Conference: July 9–13, 1990 Palais Des Congrès — Paris — France* (Springer Netherlands, Dordrecht, 1990) pp. 757–760.
- [29] W. Hsu and A. R. Brown, 2007 IEEE International Frequency Control Symposium Joint with the 21st European Frequency and Time Forum , 1088 (2007).
- [30] A. Laptev, R. Korostik, A. Svishev, A. Andrusenko, I. Medennikov, and S. Rybin, in *2020 13th International Congress on Image and Signal Processing, BioMedical Engineering and Informatics (CISP-BMEI)* (2020) pp. 439–444.
- [31] N. Srivastava, G. Hinton, A. Krizhevsky, I. Sutskever, and R. Salakhutdinov, *Journal of Machine Learning Research* **15**, 1929 (2014).
- [32] S. Davis and P. Mermelstein, *IEEE Transactions on Acoustics, Speech, and Signal Processing* **28**, 357 (1980).
- [33] S. Boyd and L. Chua, *IEEE Transactions on circuits and systems* **32**, 1150 (1985).
- [34] C. V. Jutte and S. Kota, *Journal of Mechanical Design* **130** (2008).
- [35] R. R. Craig and M. C. C. Bampton, *AIAA Journal* **6**, 1313 (1968).
- [36] S. Rubin, *AIAA Journal* **13**, 995 (1975).
- [37] P. Van der Valk, *Model Reduction and Interface Modeling in Dynamic Substructuring: Application to a Multi-megawatt Wind Turbine*, Master’s thesis, TU Delft (2011).
- [38] J. Wurtz, P. W. Claeys, and A. Polkovnikov, *Phys. Rev. B* **101**, 014302 (2020).
- [39] W. H. Press, S. A. Teukolsky, W. T. Vetterling, and B. P. Flannery, “Numerical recipes in c,” (1988).
- [40] R. Miotto, F. Wang, S. Wang, X. Jiang, and J. T. Dudley, *Briefings in Bioinformatics* **19**, 1236 (2017).

Finite element method for structure simulation

The analysis of the dynamics of the phononic system starts with the finite element method (FEM) simulations. FEM is a commonly used method for numerically solving partial differential equations, such as the three-dimensional linear elasticity equation. The continuous elastic medium (the lattice of resonators) is discretised in a set of finite elements, so as to enable a numerical simulation of its response. The equations of motion for the nodes in these finite elements and the corresponding boundary conditions are collected in a set of equations that can be written in a matrix form,

$$M\ddot{\vec{x}} + K\vec{x} = \vec{f}(t), \quad (1)$$

where \vec{x} are the positions of the nodes in the finite elements, $\vec{f}(t)$ is the force acting on them, and the matrices M and K reflect their mass and stiffness properties. The size of the mass and stiffness matrices, and of the system of equations that needs to be solved in order to extract the system dynamics, directly depends on the discretization density. Relatively high precision is required in order to succeed in the speech recognition task, on the order of 10^7 degrees of freedom for the 7×7 lattice. This motivates the approach via dynamic sub-structuring, as explained in the next section.

Dynamic sub-structuring

Complex signal processing tasks such as speech recognition require tightly-controlled mechanical properties. Therefore, it is necessary to perform FEM simulations using a very fine mesh. In this work, we use 323 kDOFs per site, which adds up to roughly 16 million degrees of freedom for the total design. Such a large number of degrees of freedom presents a computational challenge, especially given that we must perform many full lattice simulations to complete a device optimization.

We address the problem of having a large number of DOFs by performing dynamic sub-structuring [35]. A lattice consisting of multiple vibrating plates is assembled from individual plates, which in turn are assembled from building blocks such as links and hole designs (Fig. 5a). While the number of plate designs is very large ($> 2.6 \cdot 10^9$), the number of different building blocks is small: 100 instances for the arms and 26 instances for the plate hole pattern. This allows us to pre-compute lumped models for those plate designs (Fig. 5b, c). Besides the time savings obtained by bypassing the meshing and matrix assembly steps at every iteration, using a pre-computed dynamical matrices allows for increased computational parallelisation. While FEM simulation is limited by the number of available software licenses, the combination of pre-computed building blocks can be performed using

open-source tools and therefore does not pose an obstacle to parallelisation.

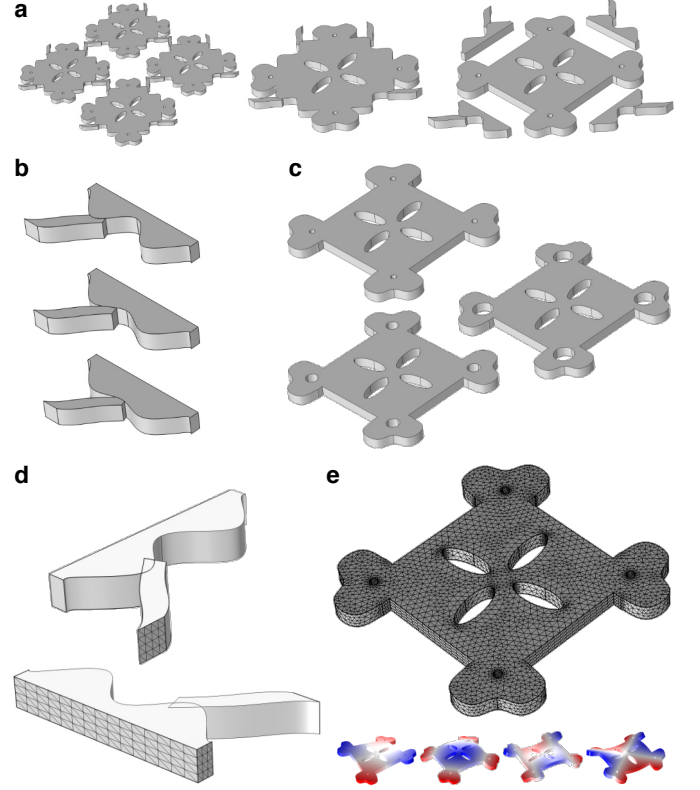


FIG. 5. Simulating a lattice by dynamic substructuring | **a** The lattice is divided in sites, which are then divided into link and resonator components. **b**, **c** The links (b) and resonators (c) are chosen from a library of pre-computed building blocks. **d** The full model is assembled by imposing matching displacements at the boundary meshes. **e** The internal (non-boundary) degrees of freedom [top] are replaced by a set of eigenmodes [bottom]. Note that not all retained eigenmodes are shown here.

To perform dynamic sub-structuring, the finite element models for every component are divided into bulk and boundary degrees of freedom. The full model is assembled by imposing matching displacements between the degrees of freedom at the interfaces between components (Fig. 5d). The bulk degrees of freedom of each building block are replaced by lattice eigenmodes obtained under free boundary conditions, following the approach by Rubin [36]. We observed that the Rubin approach, with eigenfrequency errors smaller than 0.1 % significantly outperformed the Craig-Bampton method [35], in which the bulk DOFs are replaced by eigenmodes of a structure under fixed conditions at the interface degrees of freedom, resulting in an eigenfrequency error above 1 %. This is consistent with prior reports on the low-frequency modelling of structures [37].

In this work, we model the bulk DOFs by retaining 75 eigenmodes per resonator site. The interfaces are mod-

elled using 972 DOFs. Since interface DOFs are shared between neighboring sites, each plate requires 561 individual DOFs, down from the 323 kDOFs required when performing direct FEM simulation. It should be noted that the dynamic matrices obtained by dynamic substructuring are much less sparse than those from direct finite element modelling, limiting the observed speedup of a full system diagonalisation to a factor of approximately 10. To ensure matching meshes at the interfaces between different components, we used COMSOL Multiphysics® explicit mesh functions. In complex geometries combining parametric curves and boolean operations, we observed fluctuations in the location of the boundary mesh DOFs even when the explicit mesh function was used. Using a boundary layer mesh function to improve resolution around the interface areas mitigated the problem.

Effective mass-spring model extraction

Finite element models contain a very large number of DOFs. However, the dynamics of the system at the range of frequencies of interest can be described by the small set of normal modes whose resonance frequencies lie in the relevant frequency range. For the lattices and frequency ranges considered in this work, a modal description requires one DOF per site, or 49 DOFs for the entire lattice.

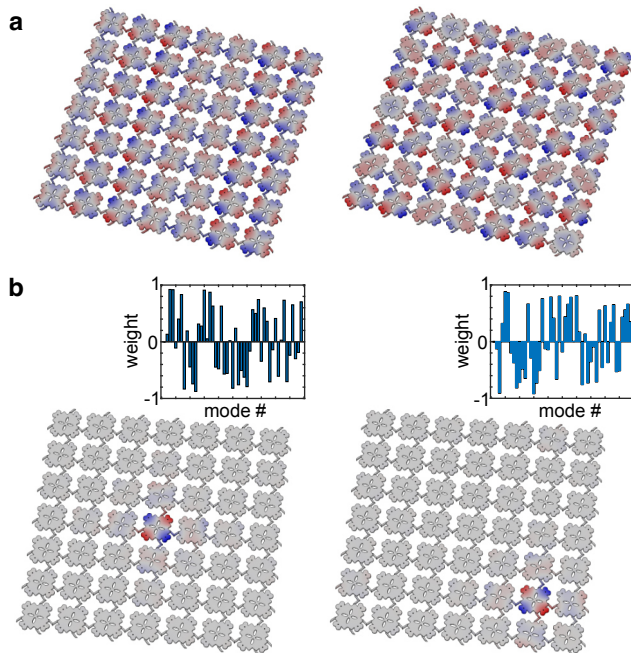


FIG. 6. Assembling a localised basis from lattice modes | **a** Example showing two lattice eigenmodes in the frequency range of interest. Lattice eigenmodes are delocalised. **b** By combining the 49 delocalised modes with suitable weights (histogram), we can assemble highly localised basis elements.

While normal modes (Fig. 6a) provide a very efficient description to simulate the dynamics of the lattice, they form an unsuitable basis for optimization. This is because the properties governing them (effective mass, stiffness and coupling force) depend on the full lattice geometry. Such full-lattice dependence has two negative consequences: First, it is very difficult to build a machine learning model that can be used to compute gradients or rapidly estimate the performance of a particular geometry. Second, determining the normal modes requires a full-lattice diagonalisation, which scales quadratically with the number of DOFs, and therefore limits the sizes of systems that can be designed. Furthermore, since normal modes extend through the whole lattice, the memory requirements for storing a normal mode basis also increase quadratically with system size, as both the number of modes, and size of the modal functions increase with lattice size.

These two disadvantages of normal modes can be avoided by describing the dynamics of the system in terms of DOFs localized at every site [Fig. 6b], analogous to atomic orbitals in Density Functional Theory. In this representation, each element of the dynamic representation depends mostly on the geometric parameters close to the site where the corresponding DOF is localized. Since the geometry surrounding any particular site can be described by a small number of parameters, the resulting simple dependence can be readily captured by a machine learning model that we use to estimate gradients and as replacement of full lattice simulations. Furthermore, since localized basis functions decay very rapidly, truncating them at a fixed radius allows for linear memory storage of basis functions.

Throughout this work, we compute the maximally localized basis by calculating the normal modes of the full lattice ψ_i , and then finding linear combinations that are maximally localized at every site j :

$$\phi_j = \sum_i a_{ji} \psi_i$$

Where the coefficients a_{ji} are found by solving the maximization problem

$$\max_{a_{ji}} [\phi_j^T P_j \phi_j],$$

where P_j is a projector with value 1 for the degrees of freedom in site j and 0 for all other degrees of freedom. The maximization is performed under the normalization condition

$$\sum_i a_{ji}^2 = 1.$$

Once the maximally-localised basis elements ϕ_i have been determined, the mass M and stiffness matrices K

for the reduced mass-spring model can be determined from the FEM mass and stiffness matrices by performing the rotation $K = \Gamma^T K_{\text{FEM}} \Gamma$ and $M = \Gamma^T M_{\text{FEM}} \Gamma$ where Γ is a matrix whose columns are the basis elements ϕ , $\Gamma = \phi_1, \phi_2, \dots, \phi_n$.

The change of coordinates introduced by Γ has the effect of isolating the dynamics of the system that takes place at the frequency range of interest, and plays an analogous role to the transformation e^S introduced by Schrieffer and Wolff [17] that we had used in prior works [16]:

$$e^S K_{\text{FEM}} e^{-S} = \begin{pmatrix} K & 0 \\ 0 & K_I \end{pmatrix},$$

where S is the generator of the transformation —computed as a series expansion [18], and K_I represents a stiffness matrix aggregating all irrelevant degrees of freedom (i.e., whose dynamics takes place outside the range of frequencies of interest). This analogy allows an alternative method to compute the effective theory based on a series expansion [16, 18], where the interaction between lattice sites is considered a small parameter. The key advantage of this approach is that it leads naturally to linear-time algorithms to determine the effective theory —as every site dynamics depends only on a fixed number of neighbors. However, the approach presents significant challenges due to the poor convergence of the series expansion [38].

Mode selection and site design

To be able to efficiently model the lattice as a mass-spring model, the design must satisfy certain conditions. First, it is necessary that every lattice site has only one vibrational normal mode in the frequency band of interest. Second, it must be possible to implement inter-site couplings of different strength values with realistic geometric parameters. Under the perturbative (weak inter-plate coupling) assumption, the normal modes of the lattice can be traced to the modes of the freely-vibrating plates [16] [Fig. 7a]. The first non-rigid-body mode is a good candidate because its boundary vibration profile alternates between positive and negative displacements and has a node. Therefore, by placing the linking beams closer or farther from the node, it is possible to reproduce a broad range of couplings.

To maximise the design space of effective mass-spring model parameters, the plates and coupling beams must be designed to allow for large inter-plate coupling strengths, while maintaining a good separation between various modes of resonance. Such separation is critical as it determines the maximum bandwidth that the structure can handle, while still being represented accurately by a simple mass-spring model [16]. These properties

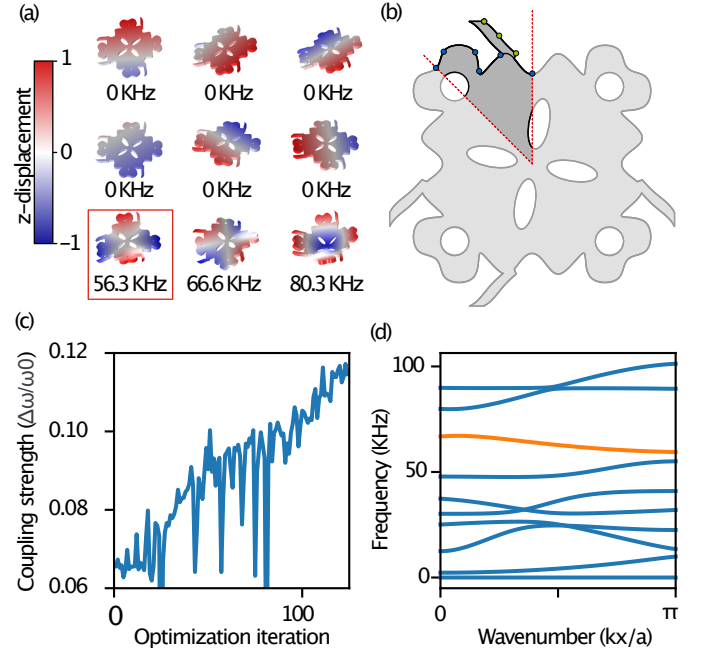


FIG. 7. Optimisation of the site design | **a** First 9 normal modes of a free-standing site. The red rectangle highlights the selected mode. **b** The site design is parameterized by a set of control points (blue dots) together with the radial dimension, rotation angle and radial location of the center elliptic holes. The coupling beams are parameterized by control points (green dots) together with a thickness parameter. **c** Evolution of the coupling strength during the site optimisation. **d** Band structure of a periodic material consisting of an optimised unit cell. The orange band arises from the selected normal mode.

are attained by numerical optimisation. We define the contour of the plates and coupling beams using splines parameterised by a set of control points [Fig. 7b]. Then, we perform an optimisation that maximises the interaction strength [Fig. 7c]. The optimisation is interrupted early to prevent the design from reaching extreme geometries (e.g. very thin beams) that would be hard to fabricate. The plate optimisation is performed using the Nelder-Mead algorithm, because it does not require gradients of the misfit, which would be hard to obtain for a spline parameterisation. To compute the misfit, we consider a periodic geometry where the site is subject to Bloch boundary conditions with wavenumber k . For this configuration, we can define a band structure [Fig. 7d] — it should be noted that in the periodic configuration, the seventh free-plate mode actually manifests as the eighth band.

The misfit for optimisation is determined by evaluating the band structure at four equally-spaced points in the Brillouin zone. Then, the spectral separation is defined

as

$$G = \sum_k \frac{1}{f_8(k) - f_7(k)} + \frac{1}{f_9(k) - f_8(k)},$$

where f_i is the frequency of the i 'th mode at wavenumber k . The bandwidth is defined as

$$\Delta\omega = \sum_k f_8(k) \cos(k),$$

and the center frequency is defined as

$$\omega_0 = \frac{1}{4} \sum_k f_8(k).$$

With these parameters, we observe that minimising a misfit of the form

$$N = -800 \frac{\Delta\omega}{\omega_0} + G + \frac{1}{64} G^2$$

produces designs with a good balance between coupling strength and frequency separation.

Time-reversal gradient calculation

The evolution of a mass-spring system can be described by an equation of the form

$$\frac{d\vec{r}(t)}{dt} = \vec{f}(\vec{r}(t), \vec{p}, t),$$

where $\vec{r} = (x_1, x_2, \dots, x_n, v_1, v_2, \dots, v_n)$ is a state vector containing the positions x_i and velocities v_i of the masses in the system, \vec{p} is a vector with the parameters of the system (masses, springs, damping factors), and t is the time.

For every audio sample, the energy transmitted is a functional of the state evolution $\vec{r}(t)$. Most neural network optimisation algorithms require access to the gradient of the output to efficiently identify the system parameters that lead to the desired response. A naive approximation to calculate this gradient involves forward-integrating the Jacobian of the state vector \vec{r} with respect to the system parameters, J_p . However, such an approach involves solving as many Ordinary Differential Equations (ODEs) as the number of parameters that the system has. An alternative approach consists of determining an adjoint field $\vec{u}(t)$, which quantifies the dependence of the energy functional on a small perturbation of the state vector $d\vec{r}$, introduced at time t . The adjoint field $\vec{u}(t)$ can be calculated by solving a single additional ODE,

$$\frac{d\vec{u}}{dt} = J_{\vec{r}}^T(\vec{r}(T-t), \vec{p}, T-t) \vec{u} + \nabla_{\vec{r}(T-t)} E.$$

The gradient of E with respect to every parameter p_i is given by

$$\int_0^T \vec{u} \cdot \frac{d\vec{f}}{dp_i} dt$$

Calculating the gradient using adjoint methods requires storing all dynamical variables $\vec{r}(t)$ at every time step. This is very memory intensive, and for this reason we divide the total number of time steps N into \sqrt{N} intervals. We perform one forward simulation, storing the dynamical variables at the start of every interval. During backward integration, every time the simulation goes through an interval boundary, \vec{r} is calculated for all the \sqrt{N} timesteps in the new interval. This has the effect of dividing the memory footprint by a factor of \sqrt{N} while increasing the computation time by one forward simulation. In practice, the time increase is lower due to the reduction in memory bandwidth, as the buffers now fit in the CPU caches.

Both forward and backward simulations are performed using a fourth-order Runge-Kutta algorithm [39] with a time step of 624.7 ns.

Machine learning model for the lattice effective theory

We found it valuable to approximate the mass and stiffness matrices separately, instead of directly predicting the dynamic matrix $D = M^{-1}K$. This preserves the symmetry of M and K and ensures that the eigenvalues of $M_{\text{ML}}^{-1}K_{\text{ML}}$ remain real. In contrast, direct learning of the dynamic matrix resulted in complex eigenvalues.

Evaluating the mass-spring dynamic matrices using FEM simulations is very expensive, as we must assemble and diagonalise matrices involving millions of degrees of freedom. To solve this problem, we construct a machine learning model to approximate the system response. The machine learning model predicts the matrices as a function of the geometric parameters.

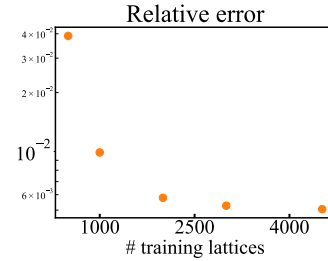


FIG. 8. Training of the machine learning model | Frobenius norm of the error between the estimated and simulated matrices $\|K_{\text{FEM}} - K_{\text{ML}}\|$, for a test set of 45 random geometries.

We express every element of the stiffness matrix K as

$$K_{ij} = a_{ij}^K + \vec{b}_{ij}^K \cdot \vec{p}_r + \vec{p}_r^T C_{ij}^K \vec{p}_r.$$

The equation for the mass matrix has the same form, substituting K by M . Here, $a_{ij}^{\{M,K\}}$, $\vec{b}_{ij}^{\{M,K\}}$ and $C_{ij}^{\{M,K\}}$ are scalar, vector and matrix parameters respectively, and are different for every matrix element $\{M, K\}_{ij}$. The vector \vec{p}_r contains the subset of geometric parameters (hole radius and beam locations) that is most relevant to the particular matrix element $\{M, K\}_{ij}$.

The relevant parameters associated to a matrix element $\{M, K\}_{ij}$ are identified by geometric proximity to the degrees of freedom i and j . Given that degrees of freedom correspond to vibrations localised at an individual plate, we can assign a distance between every geometric feature and degree of freedom. For a degree of freedom i , holes in the plate corresponding to that degree of freedom, and locations of beams that are attached to this plate, are labelled as distance 0, holes in a nearest neighbor, and beams incident to it are labelled as distance 1, while holes and beams attached to a next-nearest neighbor are assigned a 2. Elements that couple multiple sites (e.g. beams) are assigned the smallest of the two possible values. For a matrix element $\{M, K\}_{ij}$, geometric parameters corresponding to features that are at a distance of two or less are kept as relevant.

The system is trained on 5000 randomly generated training lattices, with values obtained from full FEM simulation. We tested its accuracy on a test set of 45 additional lattices, showing small residuals between predicted and simulated values [Fig. 8d].

Performance improvement through nonlinear elements

Not all binary classification problems can be efficiently solved using linear systems, but this limitation can be overcome by adding nonlinear elements in the model. Here we demonstrate such improvement for the case of the *two-three* word pair, where the linear classification performance is lowest among the simulated word pairs (See Fig. 4 of the main paper). We start the construction of the nonlinear system by taking six 7x7 linear lattices. The lattices are split in two groups containing two and four lattices respectively. The lattice outputs (center plate displacements) of the first group are labelled x_1, x_2 , while those in the second group are labelled x_3, x_4, x_5, x_6 . The result is determined by multiplying the outputs from all the lattices within each group, and adding the result, $r = x_1 x_2 + x_3 x_4 x_5 x_6$ —Nonlinearity is introduced by the signal multiplication. Experimentally, multiplications can be implemented by combining quadratic nonlinearities and linear transfer functions, $2ab = (a + b)^2 - a^2 - b^2$. For performance reasons, the lattices are modelled as 49 modal degrees of freedom —each

degree of freedom parameterised by a natural frequency and coupling constant.

Including one high-order term reduces the training set error from 38.8% to 18.6% [Fig. 9b, c], while a second nonlinear element, $r = x_1 x_2 + x_3 x_4 x_5 x_6 + x_7 x_8 x_9 x_{10}$, brings it down to 10.8% [Fig. 9b, d]. The generalisation performance of the nonlinear case is lower compared to the linear case [Fig. 9c]. This overfitting is not unexpected, as a rule of thumb in machine learning is that one requires ten times more training samples than free parameters in the model [40]. A requirement that is met by the linear problem (consisting of 161 free parameters trained over 2048 samples), but violated for the nonlinear problems (that contain 588 and 980 free parameters respectively). The problem of overfitting is known to particularly affect end-to-end trained models [30], and could be mitigated by increasing the dataset size, introducing regularisation approaches such as dropout [31], or implementing feature extraction [32].

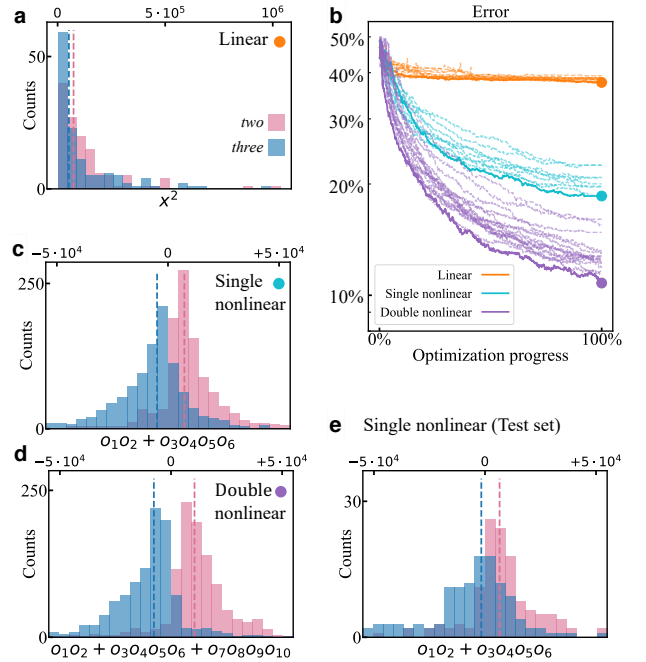


FIG. 9. Nonlinear extension | **a** The discrimination for the pair of digits *two-three* does not achieve high classification accuracies within the linear regime. **b** The inclusion of nonlinear terms increases the accuracy: Training of a linear (orange) and nonlinear (cyan, 1 nonlinear term, violet, two nonlinear terms) lattices. **c,d** Histogram of the transmitted energy for the optimized classifier between *two-three* with one and two nonlinear terms, respectively, for the training set. **e** Performance of the system with a single nonlinear term (cyan in b) on the test set. Overfitting is expected due to the relatively small number of training samples as compared to the number of parameters in the nonlinear models.

Computational methods

The design process described in this work has been implemented primarily in Python. C++ code, parallelised using POSIX threads, is used for the computationally-intensive parts of forward and gradient simulation.

Designing a device involves three different sets of codes. The first set generates the component files for the resonator bodies and links. The component files include the stiffness K_{FEM} and mass M_{FEM} matrices for the components, and metadata to identify degrees of freedom with individual component interfaces. The initial stage of component generation requires MATLAB[®] and COMSOL[®] licenses. The second set of codes builds the machine learning model used to estimate the dynamic matrices. This code is written in Python 3.7 and can be run using only open source tools. The third group of codes optimises the device geometry, which is exported as an AutoCAD[®] script. The sample design part requires access to the Google[™] Speech Commands dataset, and can optionally use the Intel[™] C++ Compiler instead of the GNU Compiler Collection (GCC). AutoCAD[®] is required to convert the optimisation output into a DXF file for fabrication. All codes used to design the sample are provided as supplementary material.

The codes used for generating the component models are in the *ComponentGeneration* folder. The sub-folder *SiteOptimisation* contains the MATLAB script *OptimiseUnitCell.m* optimises the unit cell geometry. The sub-folders *ComsolMatlab/BottomPart*, *ComsolMatlab/CenterPart*, *ComsolMatlab/LeftPart*, *ComsolMatlab/RightPart* and *ComsolMatlab/TopPart* extract the reduced models from COMSOL[®] FEM models. Each sub-folder contains two MATLAB scripts, *ExtractMatrices.m*, responsible for extracting the FEM matrices from the COMSOL[®] file, and *GenerateMatricesRubin.m*, which replaces the internal degrees of freedom by a modal description following the approach by Rubin [36]. The file *ImportCBCComponents.ipynb* contains the Python code to sort the degrees of freedom at the interface regions to ensure that full-sample matrices can be directly assembled.

Codes used for training the machine learning model can be found in the folder *MLModel*. The folder contains three files. *GenerateSites.py* generates pre-computed site components that will be later assembled into the random lattices that are used as training data for the machine learning model. *GenerateRandomLattice_7x7.py* is used for assembling the pre-computed sites into random lattices and extracting the effective properties. *InterpolateRandomLattice_7x7.py* is used to train the machine learning model using the mass-spring models generated from the random lattices.

The optimisation codes can be found in the folder *NetworkOptimisation*. The Python file *GenerateTraining-*

Data.ipynb is used to generate the dataset, by selecting, normalizing, trimming and resampling the original samples from the Google[™] Speech Command dataset. The folder *OptimiseSample* contains the code to design a lattice. It requires access to a trained machine learning model to predict lattice properties, plus the set of pre-computed structural components. The optimisation is controlled by the file *PerformOptimisation.py* and accesses the C++ files *prk.cpp* and *grk_lowmem.cpp* that compute the transmitted amplitudes and gradients respectively. The folder *SecondOrderOptimisation* contains similar files for the nonlinear problem described in Figure 9.

Lattice size selection

The 7x7 lattice size was chosen because it provides a good balance between optimization complexity and classification precision. We observed that performance degraded by 1.3 % when reducing the lattice size to 5x5, while it only improved by 0.5 % when increasing the lattice size to 9x9. This was determined by taking the best performance from a batch of 10 simulations per lattice size. For this purpose, the lattice was modelled as a mass-spring model without FEM corrections.

Sound file preparation

The sound files composing the test and training set are manually selected from the Google Speech Commands dataset. Criteria for exclusion include mislabeled samples, simultaneous audible conversations in the background or noises such as coughs, cries, animal barks, car honks, hums or buzzes. The files were selected based on their hashed file names in a way not traceable to the classification performance of any method or algorithm. The sound files are then trimmed to a duration of 0.6 s and normalised to a constant mean acoustic power.

Sample fabrication

The sample was fabricated on a double-side polished 100 mm silicon wafer. The wafer thickness is 380 μm with a measured total thickness variation across the wafer of less than 2 μm . The structures were patterned using standard microfabrication techniques. First, a 5 μm thick layer of Al was deposited on the backside of the wafer using electron beam evaporation [Fig. 7a]. The Al layer protected the structure while the silicon was etched. A layer of photoresist with 8 μm thickness was deposited on the top side of the wafer. The sample design was patterned on the photoresist using direct laser writing [Fig. 7b]. After hardening the photoresist, the silicon wafer was

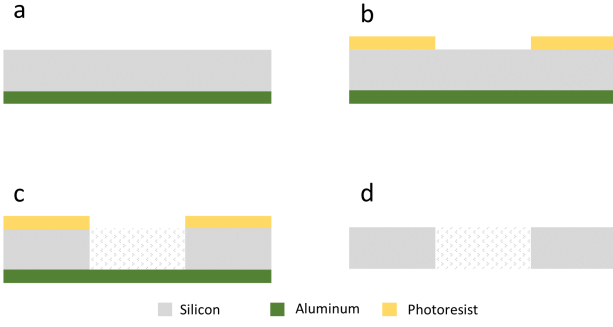


FIG. 10. Sample fabrication | **a** The fabrication started with the evaporation of Al on the backside of the wafer. **b** The wafer was coated with photoresist and the design is patterned. **c** The silicon was etched with Deep Reactive Ion Etching. **d** The photoresist and aluminum were removed by wet etching.

etched-through using Deep Reactive Ion Etching (DRIE) following a Bosch[®] process alternating etching and passivation cycles [Fig. 7c]. After the RIE, the photoresist and aluminum were removed by wet etching [Fig. 7d]. The sample was clamped between two frames to impose rigid boundary conditions. The frames were obtained following a process similar to the sample fabrication. To bond the frames to the sample, parylene was first deposited on the frames, followed by a bonding process at 350 °C .

Piezoelectric transducer calibration

Our sample is excited by 28 piezoelectric transducers (Steiner & Martins Inc, SMD063T07R111) with a

thickness-mode resonance at 3 MHz. We calibrate the transducers by measuring the vibration at 56 points along the device boundary while sending Gaussian wavepackets of the form

$$V(t) = e^{\frac{(t-t_0)^2}{2\Delta^2}} \sin(2\pi f_c t),$$

where $\Delta = 15.43\mu\text{s}$ is the pulse width and $f_c = 71.28\text{ kHz}$ is the pulse center frequency. We then Fourier-transform the measured vibration velocity recordings at the boundary points. At every frequency, we define the calibration function by finding the combination of transducer excitation signals that results in the required amplitude at the measured boundary points. Since the number of excitation channels is smaller than the number of measured points, the calibration is done as a least-squares problem using a Moore-Penrose pseudoinverse. To prevent the calibrated excitation amplitude to diverge at higher and lower frequencies, the calibration is only performed between 52 kHz and 90 kHz. Beyond this range, the calibration amplitudes and phases are kept constant. Furthermore, during experiments, the output signal is band-passed between 10 kHz and 110 kHz to prevent damaging the transducers.